NeuroImage **11,** 668–683 (2000)
doi:10.1006/nimg.2000.0561, available online at http://www.idealibrary.com on IDEAL®

Application of Cortical Unfolding Techniques to Functional MRI of the Human Hippocampal Region

Michael M. Zeineh,*† Stephen A. Engel,‡ and Susan Y. Bookheimer*,[1]

*Ahmanson–Lovelace Brain Mapping Center, University of California at Los Angeles, 660 Charles E. Young Drive South, Los Angeles, California 90095-7085; and †Interdepartmental Neuroscience Ph.D. Program, Medical Scientist Training Program, UCLA School of Medicine, and ‡Department of Psychology, University of California at Los Angeles, Los Angeles, California 90095-1563

Received September 13, 1999

We describe a new application of cortical unfolding to high-resolution functional magnetic resonance imaging (fMRI) of the human hippocampal region. This procedure includes techniques to segment and unfold the hippocampus, allowing the fusiform, parahippocampal, perirhinal, entorhinal, subicular, and CA fields to be viewed and compared across subjects. Transformation parameters derived from unfolding high-resolution structural images are applied to coplanar, functional images, yielding two-dimensional "unfolded" activation maps of hippocampi. The application of these unfolding techniques greatly enhances the ability of fMRI to localize and characterize signal changes within the medial temporal lobe. Use of this method on a novelty-encoding paradigm reveals a temporal dissociation between activation along the collateral sulcus and activation in the hippocampus proper.

Key Words: **fMRI; hippocampus; unfolding; memory; medial temporal lobe; imaging.**

INTRODUCTION

A crucial discovery in the study of human memory linked bilateral lesions of the hippocampus (HC) with an inability to consolidate new memories (Milner, 1958). Experimental lesions in other animals, as well as single-unit recordings of HC neurons in rats, monkeys, and humans, further support the importance of this region in memory formation (O'Keefe *et al.*, 1978; Squire, 1992; Rolls *et al.*, 1995; Fried *et al.*, 1997).

From these previous findings, one would expect functional imaging techniques such as PET and fMRI to show activation of the hippocampus in memory tasks.[2] However, the literature offers inconsistent reports of such activation and little insight into the specificity and functional anatomy of the hippocampus (McCarthy, 1995; Ungerleider, 1995; Desgranges *et al.*, 1998). Several studies have reported increases in signal intensity in the HC, corresponding to increases in blood flow, for novel versus previously presented stimuli (Tulving *et al.*, 1994a, 1996; Stern *et al.*, 1996; Gabrieli *et al.*, 1997). However, whether these effects involve hippocampus proper (hippocampal CA fields, dentate gyrus, and subiculum) or whether they involve only adjacent medial temporal structures, such as the parahippocampal cortex, is unclear. Other studies have found that medial-temporal signal changes during encoding correlate with the accuracy of subsequent recall, though the location of this effect has varied across studies to include parahippocampal cortex, entorhinal cortex, or posterior hippocampus proper (Alkire *et al.*, 1998; Brewer *et al.*, 1998; Fernández *et al.*, 1998, 1999; Wagner *et al.*, 1998). Several researchers have found signal changes in the hippocampal region associated with route learning, though the specific locus and the relevance to memory versus visual processes have been points of controversy (Aguirre *et al.*, 1996; Maguire *et al.*, 1997, 1998; Epstein *et al.*, 1998, 1999).

In the hippocampus proper, Fernández reported activation in more posterior regions during verbal encoding (Fernández *et al.*, 1998). In addition, signal changes have been reported in the anterior subiculum during a retrieval task (Gabrieli *et al.*, 1997). However, numerous studies have failed to find expected hippocampal activity during encoding and retrieval (Ka-

[1] To whom correspondence should be addressed at the UCLA Department of Psychiatry and Biobehavioral Sciences, Brain Mapping Division, Ahmanson-Lovelace Brain Mapping Center, 660 Charles E. Young Drive, Room 205, Los Angeles, CA 90095. Fax: (310) 794-7406. E-mail: sbook@ucla.edu.

[2] "Activation" here is defined as statistically significant signal changes secondary to a change in blood flow that accompanies large changes in neuronal firing and metabolism (Roland, 1993); for PET, this is regional cerebral blood flow, and for functional MRI, this is blood-oxygen level-dependent contrast (for reviews see Cherry *et al.*, 1996; Cohen, 1996).

1053-8119/00 $35.00

pur *et al.*, 1994; Shallice *et al.*, 1994; Tulving *et al.*, 1994b; Buckner *et al.*, 1995; Fletcher *et al.*, 1995). Recent theories attempt to resolve the controversy of global medial temporal activity during memory experiments but have yet to address the possible specialization of hippocampal versus parahippocampal regions (Cohen *et al.*, 1999b).

Three major problems may explain the lack of cohesive results in functional imaging of the human hippocampus:

1. *Technological limitations coupled with complex hippocampal architecture.* Previous imaging methodologies were limited by low resolution and a low contrast-to-noise ratio. Investigators commonly average brain activation patterns across several subjects to improve sensitivity, but the hippocampus is a very small structure that is vulnerable to misregistration between subjects. Slight misregistration can produce uncertainty in signal localization and reduce effective resolution. Furthermore, the hippocampus has a complex cellular architecture; these cellular assemblies and the adjacent parahippocampal structures may have variable contributions to memory encoding. For example, lesion data from stroke victims and epileptics illustrate that the CA1 fields may be the most vital for memory performance (Zola-Morgan *et al.*, 1986; Rausch *et al.*, 1994). Heterogeneity of function within the hippocampus makes resolution an even more critical issue because studies may inadvertently average activity across differentially responsive subregions, resulting in an effective "partial voluming" of functionally different regions.

2. *Neurophysiology: baseline firing and hemodynamic response.* The hippocampus may be a constitutively active structure. In rats the hippocampus does have very high concentrations of cytochrome oxidase, indicative of high baseline metabolism (Borowsky *et al.*, 1989). However, in PET studies of humans the hippocampus does not seem to have higher glucose or oxygen metabolism than other brain regions; surprisingly, the trend is in the opposite direction (Ouchi *et al.*, 1998; Stein *et al.*, 1998). It is possible that the hippocampus works more by changing the firing pattern of a sparse network rather than changing global firing rates (Rolls, 1996; Stern *et al.*, 1999). Thus, many tasks may not generate a change in activity sufficient to create measurable metabolic differences (Fletcher *et al.*, 1995; Ungerleider, 1995). Furthermore, the hippocampal neurovasculature is not well characterized, and it is not known if the hemodynamic response is similar to neocortical areas such as visual cortex or motor cortex, which may also differ in their respective responses (Cohen *et al.*, 1999a). Consequently, current techniques based on blood flow and blood volume changes may not be applicable to the hippocampus.

3. *Paradigm design.* Although the HC is certainly involved in new memory formation in some way, little is known about the specific computations it performs. Consequently, it is difficult to optimize experimental designs to best capture where and in what manner neural activity changes in the HC.

This paper addresses the first set of technical confounds: the functional partial voluming of fMRI signal from the functionally heterogeneous microstructures

FIG. 1. Imaging and segmentation of subject 1. (A) Prescription of the 16 structural images; the red slices correspond to the 11 planes that we scanned functionally. All references to slice number are relative to the most anterior red slice. (B) Segmentation of slices 3, 7, and 10. The left side corresponds to the right side of the brain. The left column presents the high-resolution oblique coronal scans, the middle column shows the manual segmentation of white matter and CSF, and the right column illustrates the layers of gray matter. We segmented the following as "white matter": (1) white matter in the parahippocampal gyrus throughout the full rostrocaudal extent, (2) white matter on the medial aspect of the occipitotemporal sulcus, (3) CSF in the inferior horn of the lateral ventricle, and (4) the fornix. We segmented the following as "CSF": (5) CSF in the collateral sulcus and the hippocampal fissure, (6) the ambient cistern (including the wing) and the adjacent posterior cerebral artery and basal vein, and (7) the boundaries of the segmentation.

FIG. 2. Demarcation and unfolding of subject 1. PRC, perirhinal cortex; ERC, entorhinal cortex; FG, fusiform gyrus; MFV, medial fusiform vertex; PHC, parahippocampal cortex; Sub, subiculum; CA1, cornu ammonis 1; CA23DG, CA2 and 3 and dentate gyrus; CADG, CA1, 2, and 3 and dentate gyrus; CoS, collateral sulcus; AntC, anterior calcarine sulcus. (Top) Color-coded demarcations on the oblique structural slices 3, 7, and 10. The units are in millimeters. We demarcated using the following boundaries anteriorly (slices 1–4): (1a) lateral aspect of the collateral sulcus which formed the lateral boundary of the PRC; (2a) the deepest point of the collateral sulcus; (3a) medial aspect of the collateral sulcus which formed the medial boundary of the PRC and lateral boundary of the ERC; (4) the superior, medial aspect of the parahippocampal gyrus which formed the medial border of the ERC and the medial border of the subiculum; (5a) the border between CA1 and subiculum, just inferior to the middle of the hippocampal head; and (6) the border between CA1 and CA2, drawn from the end of the hippocampal fissure to the lateral ventricle, with a 45° angle with respect to the horizontal axis of the subject. Demarcation boundaries 1a–3a were shifted medially or laterally according to the depth of the collateral sulcus (Insausti *et al.*, 1998). We demarcated using the following boundaries posteriorly (slices 5–11): (1p) lateral aspect of the collateral sulcus, labeled the MFV; (2p) the deepest point of the CoS which separates the FG from the PHC; (3p) the horizontal, medial aspect of the parahippocampal gyrus which forms the border between PHC and subiculum; (5p) the border between CA1 and subiculum, just inferior to the most medial extent of the CA3 and dentate gyrus of the hippocampal body; and (6) the border between CA1 and CA2, drawn from the end of the hippocampal fissure to the lateral ventricle, with a 45° angle with respect to the horizontal axis of the subject. (Bottom) Unfolded hippocampi with projected demarcations. Gray-scale intensity corresponds to the slice from the raw anatomy; bright means the gray matter came from a posterior slice, while dark means the gray matter came from an anterior slice. The units are in millimeters.

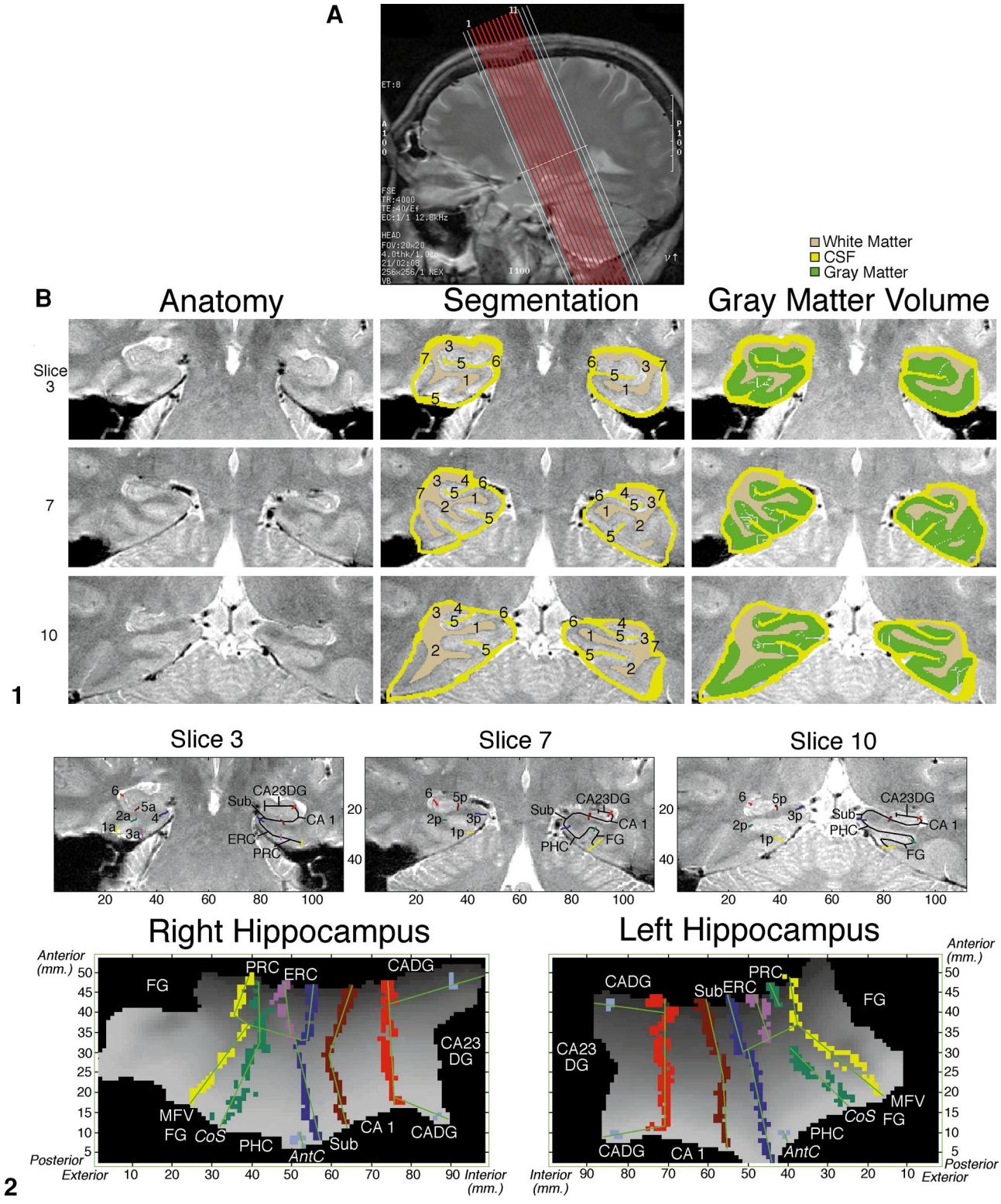
A
B
Anatomy
Segmentation
Gray Matter Volume
White Matter
CSF
Gray Matter
Slice 3
7
10
1
Slice 3
Slice 7
Slice 10
CA23DG
Sub
CA 1
ERC
PRC
PHC
FG
Right Hippocampus
Left Hippocampus
Anterior (mm.)
Posterior
Exterior
Interior (mm.)
CADG
CA23 DG
MFV
CoS
AntC
2

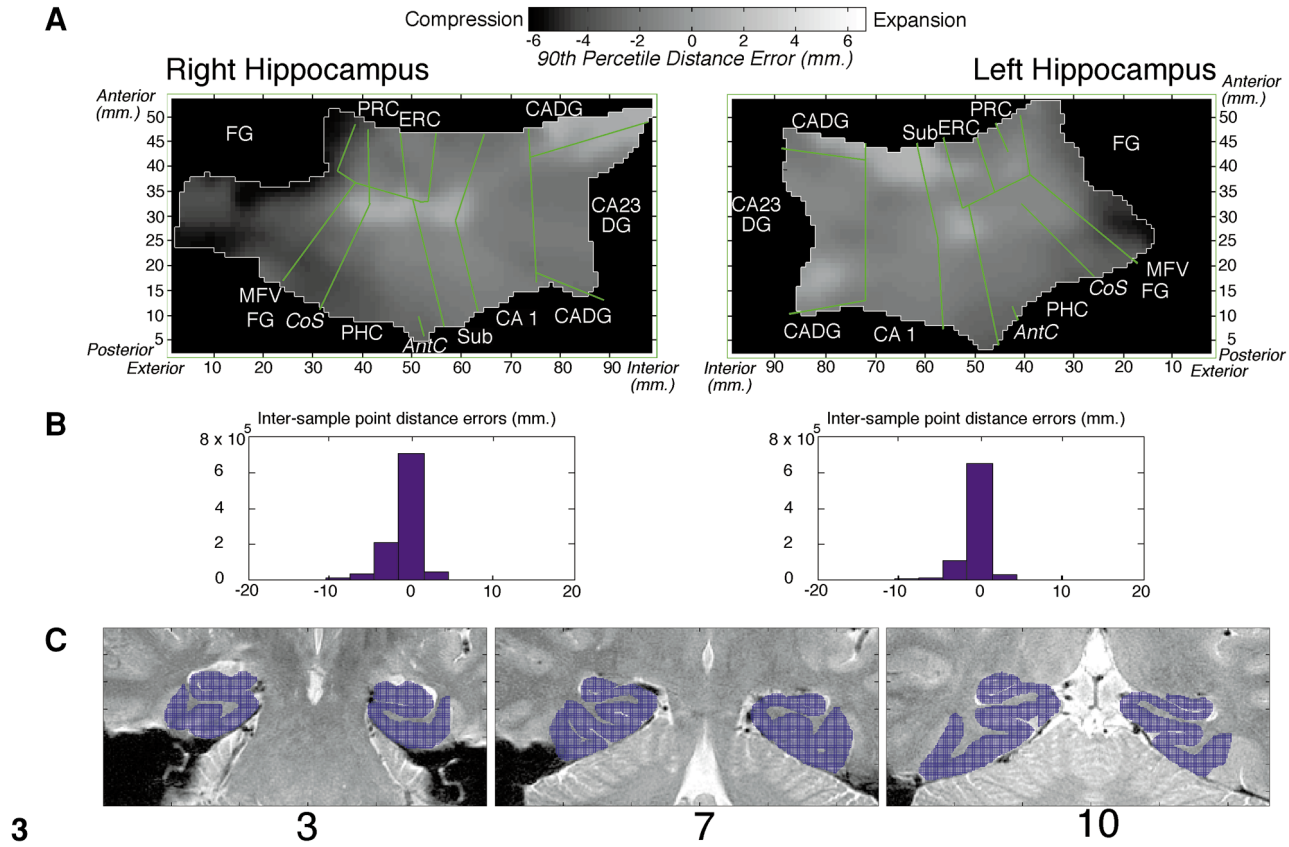

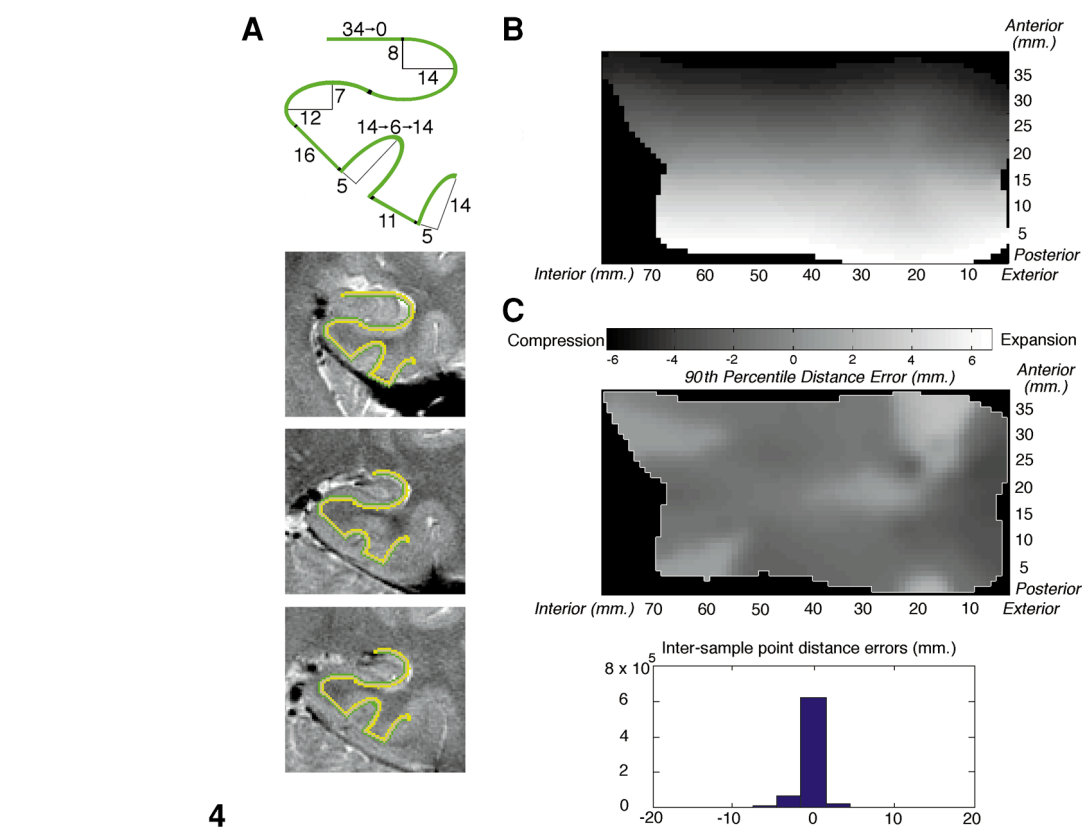

FIG. 3. Error maps for unfolding procedure on subject 1. (A) 90th percentile distance error maps. (B) Histogram of distance errors. (C) Reverse transform of flat pixels.

FIG. 4. Quantitative simulation. (A) Each plane of the simulation consisted of 7 segments of lines and ellipses that modeled a left hippocampus. The simulation was superimposed on structural data for anterior (top) and posterior (bottom) slices. Note the change in the depth of the simulated collateral sulcus. (B) The unfolded simulated hippocampus. (C) The map and histogram of 90th-percentile distance errors.

within the hippocampal region (the dentate gyrus, the CA fields, the subiculum, and the entorhinal, perirhinal, and parahippocampal cortices). We make use of cortical unfolding techniques, which were first applied to visual cortex and then to other areas of the brain, as a tool for better visualizing activity (Schwartz, 1990; Sereno *et al.*, 1995; Drury *et al.*, 1996; Engel *et al.*, 1997; Van Essen *et al.*, 1997; Dale *et al.*, 1999; Fischl *et al.*, 1999). These techniques mathematically flatten the cortical sheet, revealing functional organization that can be easily obscured in the highly convoluted cortex. In autoradiographic studies of the rat hippocampus, researchers have applied unfolding to provide for clearer depictions of anatomy and connectivity (Swanson *et al.*, 1978). Here we apply these techniques to fMRI of the hippocampal complex, generating flattened maps of the dentate gyrus, CA fields, subiculum, and nearby parahippocampal and fusiform gyri. Our implementation of this method proceeds in four phases: (1) segmenting structural images and unfolding gray matter, (2) demarcating different substructures according to anatomic atlases, (3) projecting functional images onto the flat maps to generate a flattened time series, and (4) generating two-dimensional maps of statistical significance. We demonstrate the utility of this technique in localizing fMRI signal changes during a novelty-encoding/picture-priming paradigm. This paradigm is known to elicit medial temporal activation, but the specific locus has been a point of controversy (Stern *et al.*, 1996; Gabrieli *et al.*, 1997); hence, this issue provides a natural application for our high-resolution unfolding technique. To illustrate an alternative group analysis method, we perform statistical parametric mapping (SPM) on the same data.

METHODS

Experimental Procedures

Subjects

Nine volunteers (five male, four female, right handed, ages 19–35), with no history of neurologic disorders, head injuries, psychiatric conditions, or substance abuse, participated in this study. The subjects were all right handed (Edinburgh Handedness Inventory scores of 13 or greater). All subjects provided informed consent as dictated by the UCLA Human Subjects Protection Committee. No subjects had any conspicuous abnormalities in their MRI. One subject was scanned without a bite-bar and exhibited significant motion during structural scanning. This subject was excluded and all other subjects were scanned with a bite-bar. One subject (subject 5) had additional structural scanning on a second day because of motion during the first set of structural scans. In three other subjects (subjects 6–8), we scanned the structural and functional image sets on different days to accommodate other stimulus paradigms not presented here.

Image Acquisition

Images were acquired using a GE 3.0-T MRI scanner with an upgrade for echo-planar imaging (EPI) (Advanced NMR Systems, Inc.). All subjects underwent five imaging sequences:

1. *Localizers* were obtained in the sagittal plane to identify the long axis of the hippocampus.
2. *High-resolution FSE (fast spin echo) structural images* were chosen for the segmentation and unfolding. We acquired these scans in an oblique coronal plane perpendicular to the long axis of the hippocampus as illustrated by the prescription in Fig. 1A. These used a T2 FSE pulse sequence (spin echo, TR = 3000 ms, TE = 41 ms, FOV 20, 512 × 512, ETL 8, NEX 2, 16 slices, 3 mm thick, 0 mm spacing). We chose this T2 sequence because of its high gray–white matter contrast, high in-plane resolution, and low susceptibility artifact. Voxel size was 0.391 × 0.391 × 3.00 mm. The 16 slices, covering 4.8 cm, spanned all of the head and body and most of the tail of the hippocampus for all subjects.
3. *Echo-planar structural images* (spin echo, TR = 4000 ms, TE = 54 ms, FOV 20, 128 × 128, NEX 4, 16 slices, 3 mm thick, 0 mm spacing), coplanar with the FSE structural images and echo-planar functional images, were acquired for alignment of the functional image sets with the high-resolution structural image set.
4. *Echo-planar functional images* (gradient echo, TR = 3400 ms, TE = 30 ms, FOV 20, 128 × 128, 11 slices, 3 mm thick, 0 mm spacing). We selected 11 of the 16 slices posterior to the signal loss due to susceptibility artifact from the sphenoid sinuses, covering 3.3 cm of the hippocampus.
5. *T1 weighted volume images* (SPGR, TI = 500 ms, TE = 3.7 ms, FOV 20, 256 × 256 × 124, NEX 1) were acquired to aid in visualizing sulci during segmentation.

Stimulus Paradigm

We used a picture-novelty paradigm in which the subject viewed indoor and outdoor color scenes in alternating novel and repeat blocks (Stern *et al.*, 1996; Gabrieli *et al.*, 1997). The images were of complex scenery and architecture but did not include human faces or figures. Order of alternation was counterbalanced across subjects by starting with either repeat or novel blocks. Each novel block consisted of 16 novel pictures, 8 indoor and 8 outdoor, presented in random

order with an interstimulus interval of 2.55 s, for a total block length of 40.8 s. Each repeat block consisted of 1 indoor and 1 outdoor picture presented eight times each, in random order with the same interstimulus interval as above. The same indoor picture and outdoor picture were used for all repeat blocks. The novelty paradigm consisted of five sets of these novel-repeat blocks. Total scan duration was 469.2 s, including beginning and ending rest periods of 30.6 s. In order to ensure attention to all complex scenes, subjects were instructed to press different mouse buttons for indoor and outdoor scenes.

Stimulus Presentation

Subjects viewed stimuli through magnet-compatible goggles with a color video display system (Resonance Technologies, Inc.). The stimuli were presented via a Macintosh computer driven by Macstim software (David Darby, http://porkpie.loni.ucla.edu/WhiteAnt/), which also allowed us to record response accuracy and reaction time. Subjects responded by pressing a touchpad attached to the computer (a modified "GlidePoint;" ALPS, Inc.).

Unfolding Procedure

Segmentation (Fig. 1)

The goal of the segmentation was to create a continuous gray matter volume of the hippocampus using the high-resolution structural image set. This was done by (1) manually defining "white matter" and "CSF" and (2) growing out gray matter from the white matter surface in successive layers, stopping at the CSF, thus creating a gray matter volume. Segmentation was performed on a DEC Alpha using mrGray segmentation software (Teo *et al.*, 1998; http://white.stanford.edu/wandell.html).

We first segmented white matter and CSF manually as described in the Fig. 1 legend. In order to maintain continuity of the gray matter from the subiculum to the CA fields, we classified CSF in the lateral ventricles as white matter to provide a continuous strip of white matter upon which the gray matter would rest. The boundaries of the segmented regions were delineated and defined as CSF, imposing an exterior border that isolated gray matter. To improve the quality of the segmentation, we then interpolated the images by a factor of 7 along the longitudinal axis to arrive at a more isotropic volume size of $0.391 \times 0.391 \times 0.429$ mm, and we manually interpolated the segmentation across successive slices to smooth the transitions. A region-expansion algorithm was used to grow 18 topologically connected layers of gray matter (Teo *et al.*, 1998). The maximum thickness of the surface was about 7 mm, and this covered all of the gray matter pixels of interest. The average thickness was approximately 4 mm for a typical subject. For subjects 5–8, we performed the segmentation with a larger, interpolated pixel size of $0.520 \times 0.520 \times 0.5$ mm, and we interpolated the segmentation in successive steps (first by a factor of 3, then by 2). In our experience, this reduces segmentation time without compromising resolution or data quality.

Unfolding

The goal of the unfolding is to take the gray matter volume from the segmentation, unfold it so that it is flat, and compress the volume into a thin gray matter sheet. The gray matter volumes were sampled at 1.5 mm and then computationally unfolded and flattened using mrUnfold software (Engel *et al.*, 1997; http://white.stanford.edu/wandell.html). Computation was performed on a DEC Alpha running MATLAB (The Math Works, Inc.). The algorithm produces transformations that convert 3-D volume coordinates to 2-D flattened hippocampal coordinates (the forward transform) and vice-versa (the reverse transform). Only points in the defined gray matter are projected to the flat space. However, the transformation is not one-to-one because multiple voxels in 3-D space can contribute to a single voxel in flat space. Prior work has confirmed that the algorithm produces topographically correct unfoldings with minimal levels of distortion (Wandell *et al.*, 1996).

Demarcating Boundaries on the Unfolded Map (Fig. 2)

Correlating landmarks in the high-resolution structural images with coronal anatomic atlases, we delineated boundaries of the fusiform, parahippocampal, perirhinal, entorhinal, subicular, CA1, and CA2 and 3 and dentate fields using a rule-based decision schema (see legend, Fig. 2) (Amaral *et al.*, 1990; Mai, 1997; Duvernoy, 1998). The classification rules were based upon the known correspondence between anatomical landmarks visible in the coronal FSE images and cytoarchitectonics. While these associations are only approximate in their correlation with the histology, the rule-based system ensures consistency across subjects within the sample. Additionally, to aid in visualization, we marked the collateral sulcus, the anterior calcarine sulcus, and the medial vertex of the fusiform gyrus.

The border between the parahippocampal cortex (PHC) and the perirhinal/entorhinal cortices (PRC/ERC) was defined in relation to the head of the hippocampus. On straight coronal sections, the posterior border of the ERC is approximately coplanar with the anterior border of the lateral geniculate nucleus (Amaral *et al.*, 1990). The hippocampal head begins approximately 1–3 mm anterior to that border (Amaral *et al.*, 1990; Mai, 1997; Insausti *et al.*, 1998). Since our images were oriented at roughly a 25–30° angle relative

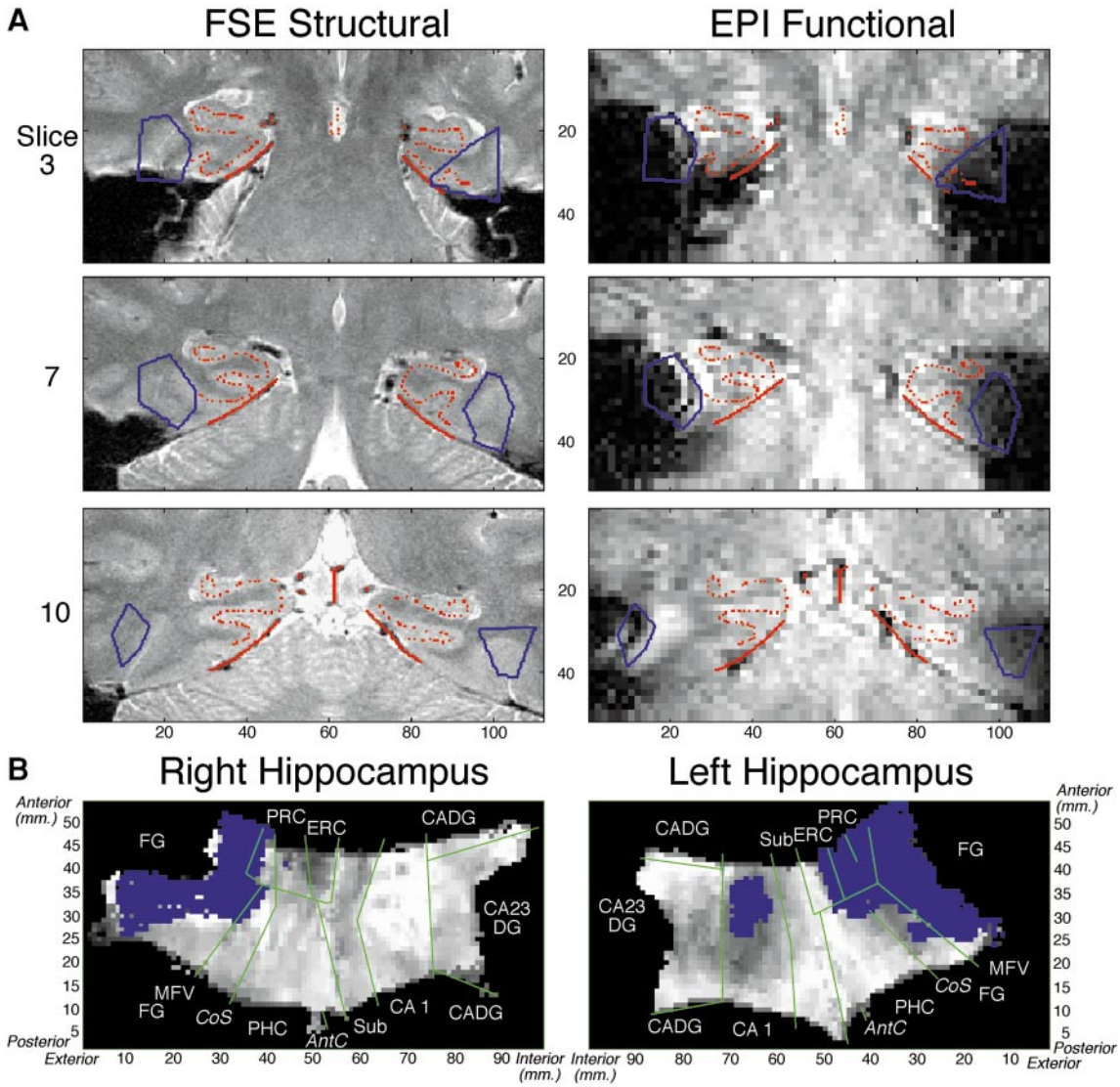

FIG. 5. EPI integration for subject 1. (A) Alignment between structural and functional image sets with fiducial points marked in red and susceptibility artifact regions outlined in blue. (B) Projected maps of susceptibility artifact. The green demarcations were imported from Fig. 2.

to the vertical, we identified the most posterior slice containing any portion of the head of the hippocampus as the posterior boundary of the ERC. The perirhinal cortex was defined as extending from the lateral to the medial aspect of the collateral sulcus, lateral to the entorhinal cortex, and these perirhinal boundaries were shifted according to the depth of the collateral sulcus (Insausti *et al.*, 1998).

There are limitations to our ability to separate the architectonic regions at this resolution. The dentate gyrus (DG) is indistinguishable from the adjacent CA fields, so that entire region was labeled CA23DG. In addition, at its most anterior and posterior ends, the CA1 field is inseparably mixed with the other CA fields and the DG. We demarcated this region CADG; anteriorly, we marked the first slice containing the full portion of the hippocampal head (generally slice 2 or 3), and posteriorly, we marked the slice in which the fornix begins its superior ascent (slice 11 or 12), which is near the anterior end of the anterior calcarine sulcus. Because anteriorly the hippocampus bends medially and curls inward, the most anterior part of the hippocampal formation in coronal sections is the subiculum. However, this most anterior portion of the subiculum was not imaged functionally because of susceptibility artifact, and hence the very anterior subiculum was neither segmented nor demarcated.

The gray matter surrounding the very posterior portion of the collateral sulcus is termed the retrosplenial cortex and is thought to be an important structure in memory formation (Shallice *et al.*, 1994). In these experiments, the retrosplenial cortex was present only in

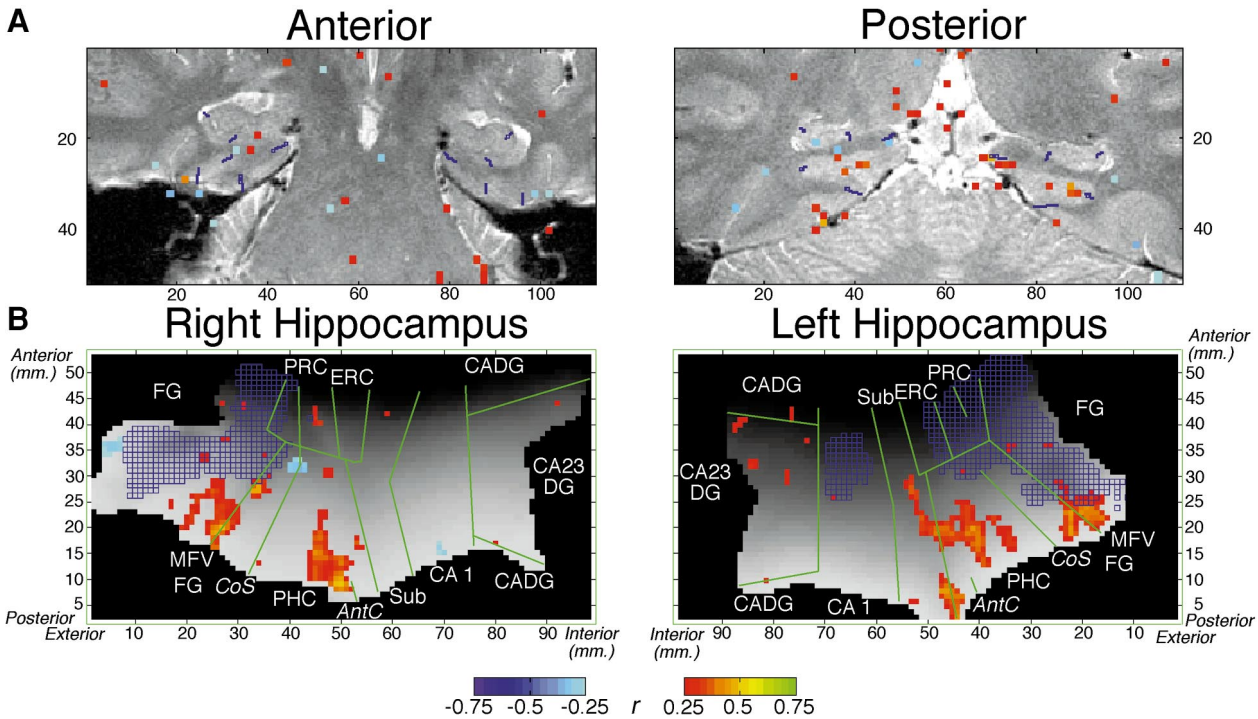

FIG. 6. Activation map of subject 1. Red refers to activation (increased signal with novelty), and light blue to deactivation (decreased signal with novelty), relative to the repeat condition. (A) Viewed in coronal section. The dark blue pixels indicate subregion demarcations similar to those in Fig. 2. (B) Viewed on the flat maps. Dark blue pixel outlines indicate pixels demarcated with susceptibility artifact as in Fig. 5.

a subset of subjects in the most posterior slice; unfortunately, data in the most extreme slices were lost in the motion correction process. For this reason, this study did not incorporate the retrosplenial cortex into the demarcation. Future studies with more posterior slices may consider labeling the region.

These demarcations were projected onto the flattened hippocampi via the transformation derived from the unfolding algorithm. We manually traced these demarcations on the flat maps for use as final region boundaries in Figs. 3, 5, and 6.

Distance Errors (Figs. 3A and 3B)

Maps of errors or distortions that occur during unfolding are useful for monitoring the accuracy of the unfolding procedure (Carman *et al.*, 1995; Drury *et al.*, 1996; Fischl *et al.*, 1999). Distance errors are defined as the difference between any two points along the 3-D manifold compared to the 2-D flat map; the unfolding algorithm attempts to minimize these errors. According to our sign convention, negative distance errors are indicative of compression, whereas positive distance errors are indicative of expansion during the unfolding process. For each pixel in the flat map, we calculated the distance error with every other pixel in the flat map and produced a histogram of these errors (Fig. 3B). In order to produce an image of distance errors, we computed the 90th percentile of each pixel's distance errors and plotted it as image intensity (Fig. 3A).

Reverse Transform (Fig. 3C)

To show that the reverse transformation calculated by the unfolding algorithm preserves the original hippocampal shape without distortion, we executed the reverse transformation of all pixels on the flat map, producing Fig. 3C. This is analogous to refolding the hippocampus.

Simulated Segmentation and Unfolding (Fig. 4)

To further validate that unfolding the hippocampus results in acceptable levels of distortion, we simulated a segmentation of geometric figures with known arc lengths to compare analytic distance with computationally unfolded distance. The simulated segmentation is depicted in Fig. 4A and exhibited slice-to-slice variation only in (1) the length of the hippocampal head, which decreased linearly from 34 pixels anteriorly to 0 pixels posteriorly, and (2) the depth of the collateral sulcus, which in the middle of the segmentation decreased from 14 to 6 pixels and increased back to 14 pixels. The simulated segmentation was unfolded and error maps were produced by the same method and

with the same parameters as the actual segmentation (Figs. 4B and 4C).

Integration of EPI

Image Processing of Functional MRI Data

We performed motion correction by aligning all functional volumes to the first volume time point using automated image registration (AIR) (Woods *et al.*, 1998). Motion was minimal in all subjects, less than the size of a pixel (1.5 mm) within the medial temporal lobe, as measured by computing the maximal displacement of fiducial points in the hippocampi by the AIR transformation matrix for each slice.

Each functional image was nearest-neighbor interpolated to match the spatial resolution of the FSE structural images (by a factor of 4 for subjects 1–4, 3 for subjects 5–8). For each of these time points, the gray matter was projected on the unfolded map using the forward unfolding transformation parameters (derived from the unfolding of the coplanar high-resolution FSE images), thus creating a flattened time series representation of the data. Intensity was averaged across the multiple layers that were projected onto the same pixel in the flat map.

Alignment of Functional and Structural Image Sets (Fig. 5A)

The structural and functional images were acquired in the same oblique coronal plane. With use of the bite-bar, motion was minimal so through-plane alignment was unnecessary. We shifted the high-resolution EPI structural image set in-plane to match the high-resolution FSE structural image set using easily identifiable fiducial points such as the posterior cerebral artery, lateral ventricle, and boundaries of the brain. This corrected a shift in center location between conventional and echo-planar images imposed by our scanner. Since the EPI functional image time series are coregistered with the EPI structural image set, we applied the same corrective shift to the EPI functional image time series. We fine-tuned the alignment by drawing and overlaying outlines of the hippocampal structure (shown in red in Fig. 5A) and shifting the EPI functional image time series accordingly.

Susceptibility Artifact Mapping (Figs. 5A and 5B)

Regions of large local variation in the magnetic field exhibit a signal loss called susceptibility artifact; this loss is projected onto the unfolded maps. To approximately establish the limits of artifact-free data, we manually demarcated all places where the anatomy in the FSE structural images was obscured in the EPI functional images (areas outlined in blue in Fig. 5A). Specifically, we marked the edge of the ring artifact on the right hemisphere and all places where the sulci were not easily visible due to signal loss in the left hemisphere. The projection of these demarcations produces a rough map of susceptibility artifact. Figure 5B shows a flattened time series image with a superimposed susceptibility demarcation. Additionally, the flat time series image illustrates the loss of the anterior and posterior oblique-coronal slices secondary to motion correction.

Functional Data Analysis

Individual Flattened Activation Images

First, we smoothed the flattened time series image with a 9-pixel Hanning filter. Since the flat resolution was at 1 mm while raw pixel size was at $1.5 \times 1.5 \times 3$ mm, this constituted a minimal loss in resolution. Next, the experimental paradigm, an ABABABABAB design, was convolved with a model of the hemodynamic response function that takes into account the phase lag and gradual rise and fall (Cohen, 1997). The resulting function was then correlated with the MR signal intensity for each pixel in the image using Pearson's correlation coefficient (r). Those pixels exceeding a statistical threshold of $r = 0.25$ were color-coded and superimposed onto the flat maps with demarcated boundaries.

Group Analysis of Anatomic Regions of Interest

In order to perform a group analysis of the flattened data, we used the subregion demarcations to manually select nonoverlapping regions of interest (ROIs) on the flat maps; these ROIs covered the fusiform gyrus (FG), PHC, PRC, ERC, subiculum, CA1, and CA23DG in each subject. No pixels were excluded due to statistical thresholding, but pixels demarcated as having susceptibility artifact were excluded. For each region and in each subject, the time courses from all pixels were averaged into a composite time course for the region. In order to correct for signal drift and to normalize the signal, we divided the time course by a linear trend fit to the rest and repeat conditions.

We computed correlations between the individual ROI time courses (for each hemisphere and averaged across hemispheres) and the previously described model of the paradigm. To identify activations in subregions that were consistent across subjects, we performed two-tailed t tests on these correlations to test if their means were significantly different from zero. To observe if activation magnitude increased over time, we computed the correlation for the first two novel and repeat blocks as well as the last two novel and repeat blocks and subtracted one from the other. Two-tailed t tests were again used to test if the differences between late and early correlations were significantly different from zero. For display, we averaged these time courses across subjects and hemispheres (Fig. 8).

Statistical Parametric Mapping

For a conventional group analysis of the data, we performed SPM. Using a six-parameter rigid-body model with AIR, we normalized the echo-planar structural images of the same eight subjects to a T2-weighted echo-planar atlas in Talairach space (Woods *et al.*, 1999). Combining this normalization with the results of motion correction, we resliced each of the images for each subject into the atlas space. After performing 3-D Gaussian smoothing with a 6-mm full-width half-maximum kernel, we imported these data into SPM99 and analyzed the novel–repeat contrast, ignoring the beginning and rest ending blocks, with a smoothed boxcar reference function and no covariates. We created *t* maps using an uncorrected threshold of $P = 0.0001$ and an uncorrected spatial extent threshold of 10 voxels.

RESULTS

Structural Unfolding

Demarcated Flat Maps

Each of the eight subjects showed similar shapes and bilaterally symmetric flat maps (subjects 1–8 shown in Figs. 2 and 7). In subject 1, the right flat map is wider than the left because of greater folding and more segmentation of the fusiform region; however, the hippocampus proper seems very similar in size and topology between the left and the right. The sizes of the other regions were similar across subjects, and the flat maps easily differentiated the major substructures of the hippocampal formation (CA fields, subiculum, and entorhinal cortex) and nearby structures (parahippocampal, fusiform, and perirhinal cortices).

Distance Error Maps

The distance error maps and histograms of Figs. 3A and 3B illustrate that the distortion introduced by unfolding a real hippocampus was minimal; most of the pixels had a 90th percentile distance error of less than 5%.

Reverse Transform

The reverse transform of Fig. 3C shows that the flat maps, when refolded, cover all of the pixels of interest in the original hippocampal structure. Thus, the unfolding algorithm did not introduce significant distortions into the reverse transformation.

Simulation

The analytic in-plane arc length of the simulated hippocampal region was 71 mm in the most anterior section and 58 mm in the most posterior section. The measured arc lengths before unfolding were 75 and 64 mm, respectively, being greater than the analytic lengths due to digitization. After unfolding, the arc lengths were 76 and 65 mm, respectively. Hence, distance along the pixelated manifold is accurately preserved.

Figure 4B illustrates that the flattened simulation has a simple unrolled appearance with a linear extent to the interior hippocampal head as would be expected from the simulated segmentation. Figure 4C illustrates the distance errors, which were minimal throughout the simulation. Minor expansion took place near the middle of the map where the collateral sulcus was shallow, and both compression and expansion occurred on the edges. This simulation thus shows that unfolding process applied to the basic hippocampal structure maintains local and global distances and minimizes distortions.

EPI Integration

Alignment of Structural and Functional Image Sets

Despite the differences in resolution between structural and functional image sets, Fig. 5A illustrates that, in regions devoid of susceptibility artifact, the outlines and landmarks on the structural images appeared to accurately define the same structures on the functional images.

Susceptibility Artifact Mapping

Susceptibility artifact limited our ability to determine functional activity in the anteriormost portions of the hippocampal region and in portions of the fusiform gyrus (Fig. 5B). The extent of susceptibility artifact differed across subjects and between hemispheres (shown as the dark blue, hollow squares, Figs. 6 and 7).

Experimental Results

Behavioral Results

Across all subjects, response accuracy in identifying whether a scene was indoor or outdoor was extremely high (>96%).

Individual Flattened Activation Images

Figure 6 shows the location of significantly activated pixels on the original coplanar structural FSE images (Fig. 6A) and the flattened hippocampal maps (Fig. 6B) for subject 1. Comparing images acquired while subjects viewed novel pictures to those acquired when subjects viewed the same picture repeatedly, there were extensive areas of relatively greater MR signal intensity in the parahippocampal and fusiform cortex. The pattern of significant activation is difficult to discern in the single-slice data, whereas in the flat maps,

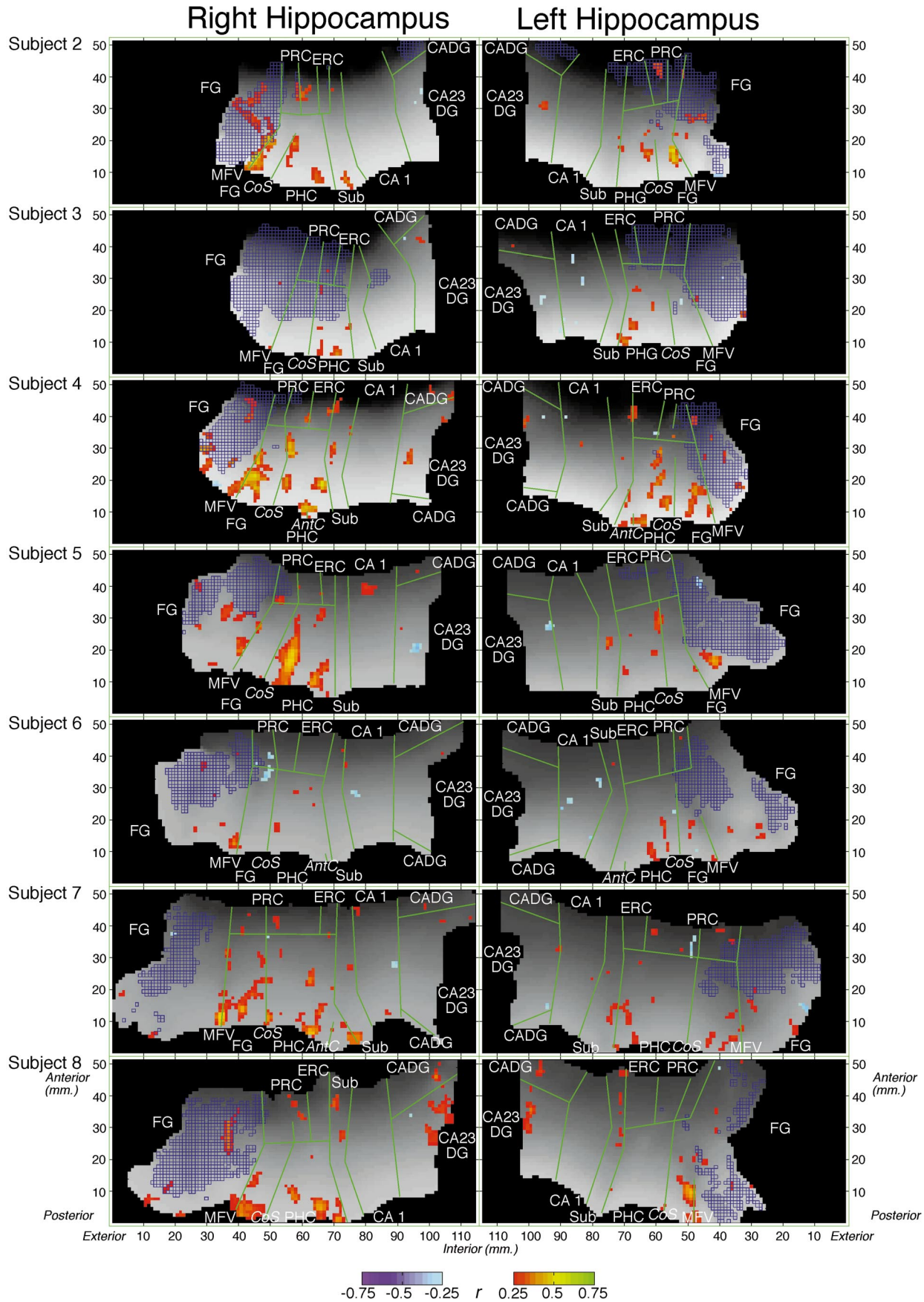

FIG. 7. Flat activation maps for subjects 2–8.

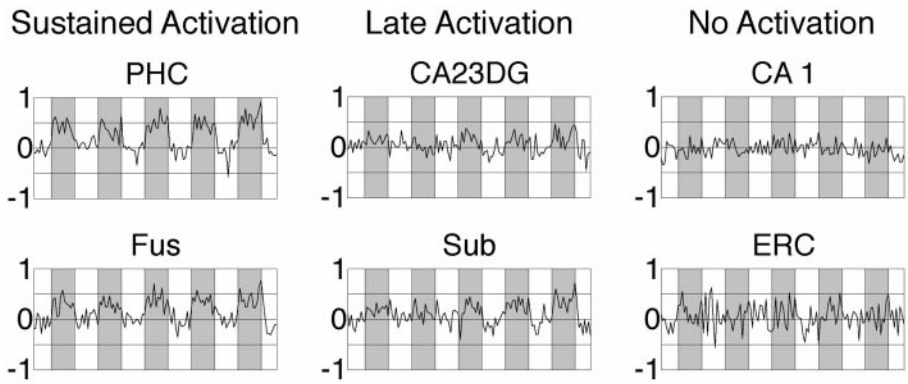

FIG. 8. Time series for group analysis of ROIs averaging across subjects and hemispheres. No statistical thresholding was involved in pixel selection, but pixels with susceptibility artifact were excluded. The vertical scale is in units of percentage change, and the horizontal axis represents novel (shaded background)–repeat (white background) blocks. The PRC time course (not shown) was similar in appearance to that of the ERC.

the anterior–posterior continuity of the activation is readily apparent. While one could visualize this continuity of activation simply by reslicing the images obliquely at the appropriate angle, it would be not only time consuming to find the angle but also too specific to apply to other activations in which the anatomy is oriented differently. The unfolding procedure, on the other hand, inherently addresses such anatomic variability to help visualize contiguity. While the anisotropic voxel size may result in a greater apparent longitudinal extent to activations (e.g., 3 1-mm voxels), the activation in this subject clearly extends across several slices (10 1-mm voxels) to span a centimeter in the flat map. In the left hippocampus, the activation extended into the subiculum, and a small number of voxels were active in CA23DG. There were no other foci of increased MR signal intensity unambiguously located in the hippocampus proper.

Figure 7 shows flat maps of activation from the other seven subjects. All subjects had similar results with distinct activation on one or both sides of the collateral sulcus. While two subjects (3 and 6) had a small amount of activation limited to the collateral sulcus, the other subjects had larger and more widespread

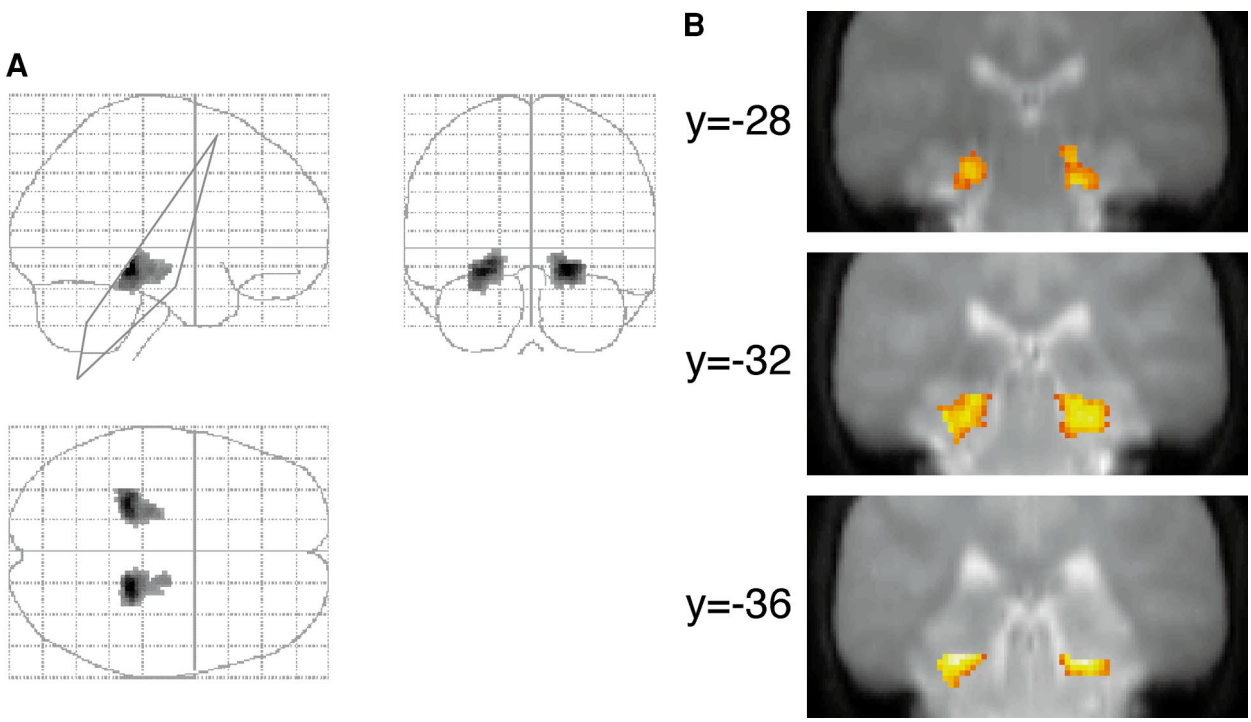

FIG. 9. Statistical parametric activation maps for subjects 1–8. (A) The gray outline in the lateral view indicates the final volume covered after normalization and subject averaging. (B) Coronal view of three slices superimposed on T2 atlas.

TABLE 1

Mean ± (SE) of Correlation Values by Region

	CA23DG	CA1	Sub	ERC	PRC	PHC	FG
Left	0.132*	−0.006	0.176**	0.012	0.060	0.361***	0.292***
	(0.055)	(0.073)	(0.048)	(0.042)	(0.038)	(0.057)	(0.042)
Right	0.112*	0.021	0.191**	0.133*	0.144	0.408***	0.260*
	(0.039)	(0.053)	(0.052)	(0.055)	(0.061)	(0.059)	(0.080)
Both	0.155*	−0.004	0.235**	0.095	0.122	0.479***	0.349**
	(0.051)	(0.068)	(0.049)	(0.065)	(0.061)	(0.045)	(0.070)

Note. FG, fusiform gyrus; PHC, parahippocampal cortex; PRC, perirhinal cortex; ERC, entorhinal cortex; Sub, subiculum; CA1, cornu ammonis 1; CA23DG, CA 2 and 3 and dentate gyrus. *P* values are for uncorrected, two-tailed *t* tests calculated from the mean and variance of the subjects' correlation values.

* $P < 0.05$.
** $P < 0.01$.
*** $P < 0.001$.

activation foci that included the subiculum and CA23DG.

Group Analysis of Anatomic Regions of Interest

Figure 8 shows the time series for all nonartifact pixels in the ROIs averaged across all eight subjects and hemispheres, and Table 1 shows the average correlation of each ROI with the experimental model. Strikingly, the effect is very clearly seen in the time courses and correlations for the PHC and FG without any statistical thresholding. Thus, with flat mapping we are able to achieve the statistical sensitivity of group data while maintaining the resolution needed to distinguish between subregions. Interestingly, the subiculum and CA23DG generated sizeable signal changes only in the latter part of the run. We quantified this by computing the correlation separately for the first two and last two blocks and subtracting the two correlation values, with the results shown in Table 2. While the fusiform and parahippocampal activations are unchanged ($P > 0.2$), the left subicular ($P = 0.006$) and left CA23DG ($P = 0.013$) activations were greater for the last two blocks compared to the first two blocks. The ERC, PRC, and CA1, on the other hand, exhibited little activation of any kind.

Statistical Parametric Map

Figure 9 and Table 3 show the *t* scores and activation map for the novel–repeat contrast in SPM99. There is a large, bilateral medial-temporal activation that centers in the parahippocampal/fusiform gyrus, consistent with the unfolding results.

DISCUSSION

Unfolding the Hippocampal Region

We have described a novel method for processing and displaying high spatial resolution fMRI of the hippocampal region. The convoluted anatomy of the hippocampus in combination with its small size makes localization of activation in the region potentially unreliable. Our method addresses these problems by scanning at high resolution and unfolding the complicated hippocampal anatomy, thus allowing for accurate functional localization within the hippocampal substructures. With current limitations of slice resolution and slice thickness, it is not yet possible to separate the subregions of the hippocampus completely in the most anterior and posterior segments. Nevertheless, by reducing variance attributed to structural dif-

TABLE 2

Mean ± (SE) of Late Correlations − Early Correlation by Region

	CA23DG	CA1	Sub	ERC	PRC	PHC	FG
Left	0.218*	0.062	0.185**	0.113	−0.006	0.069	0.130
	(0.066)	(0.088)	(0.047)	(0.093)	(0.087)	(0.093)	(0.115)
Right	0.158	−0.045	0.167	−0.012	−0.039	0.023	−0.013
	(0.093)	(0.093)	(0.084)	(0.057)	(0.058)	(0.078)	(0.075)
Both	0.217*	−0.015	0.250**	0.015	−0.021	0.094	0.050
	(0.090)	(0.098)	(0.065)	(0.074)	(0.051)	(0.084)	(0.101)

Note. See legend to Table 1.

TABLE 3

SPM Activation Clusters of Increased Signal Intensity during Novel Stimuli Compared to Repeated Stimuli

Region	Maximally activated voxel coordinates (x, y, z)	t value
R parahippocampal gyrus	20, −34, 12	10.31
R parahippocampal gyrus	16, −16, −14	5.33
L parahippocampal gyrus	−26, −36, −14	9.61
L parahippocampal gyrus	−22, −24, −12	6.43
L fusiform gyrus	−32, −40, −20	6.37

ferences between subjects, we can better localize activations. Indeed, using this method, we were able to reveal a complex pattern of activity in the different subregions of the hippocampus in a novelty-encoding paradigm.

The group analysis using SPM effectively revealed the same parahippocampal and fusiform activations as did the flat maps, though the flat maps provide more detailed information on activation in the hippocampal subregions. While methods such as SPM are well suited to whole-brain mapping across subjects, flat mapping with subject averaging offers an additional advantage for the high-resolution analysis of a small region of the brain.

We performed the demarcation under the guidance of several atlases, one of which has coronal MRIs (Duvernoy, 1998). Additionally, others have performed MR segmentation of the entorhinal and perirhinal cortex and have described the correlation with histology (Insausti *et al.,* 1998); we incorporate the criteria identified in their work into our demarcation guidelines. The reproducibility of the method is illustrated by the comparability of the flat demarcations and the activation patterns in both hemispheres across subjects; this is similar to the validation of flattening methods performed by other investigators (Dale *et al.,* 1999).

Unfolding a model hippocampus clearly showed that the distance errors involved are minimal. Similarly small distance errors were present in the error maps of the real unfolded hippocampi. Thus, the distortions introduced by unfolding the hippocampus are unlikely to cause any major difficulties.

Echo-planar and conventional images differ slightly in their distortion characteristics in a way that affects the accuracy of superimposition. Nevertheless, Fig. 5 demonstrates that we are able to achieve an alignment adequate for mapping of subregions. Corrective methods to reduce this distortion could be applied to further improve the alignment (Jezzard *et al.,* 1995; Cohen, 1997). Another difficulty inherent to echo-planar imaging is the high susceptibility artifact present in the medial temporal lobe. Using susceptibility artifact mapping, we display where data are artifact-free for improved visualization and quantitation. Different functional pulse sequences, such as asymmetric spin echo, should reduce susceptibility (though at the cost of contrast).

At present, this method is labor intensive. The entire procedure takes approximately 16 h of manual work and 12 h of computation. We expect to better automate the procedure to reduce the amount of manual work required.

Novelty Activations

One of the difficulties in the literature has been to observe unequivocal activation of the hippocampus proper; we have developed this technique specifically to address this uncertainty and dissociate responses in the heterogeneous substructures. This picture-priming paradigm was originally reported to show signal changes that extended into the hippocampus (Stern *et al.,* 1996). Other investigators have used the more general term "hippocampal region" to denote brain activity near, but not necessarily within, the HC formation. Different regions within the HC as well as nearby cortex (PHC, FG) have uniquely specialized functions; the fusiform and parahippocampal gyri in particular have been implicated in aspects of complex visual processing (Corbetta *et al.,* 1991; Allison *et al.,* 1994; Kanwisher *et al.,* 1997; Epstein *et al.,* 1998). Higher signal during the presentation of novel pictures may reflect increased visual form processing, rather than reflecting a declarative memory process per se. If we are to understand what paradigms differentiate these structures and what contribution each makes to memory and related processes, delineating the boundaries of functional activation is essential.

In the present study, we found hippocampal and extrahippocampal activations with distinct temporal characteristics. The fusiform and parahippocampal gyri were strongly active throughout the run, while the subicular and CA23DG subregions were active only toward the end of the run. On the basis of anatomy, one might conclude that the fusiform gyrus is performing visual processing, and its maintained response is evidence of visual priming. The parahippocampal cortex, known to project to the hippocampus proper, may be engaged in novelty detection. However, there is no distinction in their respective time courses, so such interpretations are speculative. More importantly, we have shown a dissociation of activation between cortical and hippocampal structures; namely, that the subiculum and CA23DG show a contrast only toward the end of the paradigm. We have found the hippocampus proper to respond late during a related-words paired-associates paradigm (Wong *et al.,* 1999). One possible explanation is that early in the run the subjects are encoding the novel and repeat stimuli, whereas later in the run, the subjects are encoding only the novel stimuli, as the repeat stimuli have been exhaustively en-

coded. The present experiment alone cannot offer a complete explanation for the dynamic signal changes; more direct experimentation is required. Interestingly, CA1, a region known to be the most critical for new memory formation from epilepsy and stroke studies, exhibits no effect in this experiment.

CONCLUSION

Given the incontrovertible evidence of the importance of the hippocampus in memory, the failure to show reliable activation in memory experiments is a challenge to the field. The method presented here greatly reduces sources of anatomic variance and mislocalization using hippocampal unfolding. Applying this approach to a novelty paradigm, we have localized activations to the fusiform gyrus, parahippocampal gyrus, subiculum, and CA23DG that differ in their respective time courses. Furthermore, this method should allow future success in identifying paradigms that result in unequivocal hippocampal activation. Then, we can continue to pursue the neurophysiology and functional anatomy of the different subregions of the hippocampus using functional MRI.

ACKNOWLEDGMENTS

This work was supported by NIH National Research Service Award Grant MH12167 from the National Institute of Mental Health, NIH Medical Scientist Training Program Grant GM08042, the Ahmanson Foundation, the Pierson–Lovelace Foundation, the Jennifer–Jones Simon Foundation, and the Tamkin Foundation. Special thanks to Oi Lee Wong for her help in segmentation. We also acknowledge Brian Wandell for the use of his segmentation and unfolding software. Finally, we thank J. Mazziotta, M. Cohen, A. Toga, C. Houser, and three anonymous reviewers for their comments on the manuscript.

REFERENCES

Aguirre, G. K., Deter, J. A., Alsop, D. C., and D'Esposito, M. 1996. The parahippocampus subserves topographical learning in man. *Cereb. Cortex* **6:** 823–829.

Alkire, M. T., Haier, R. J., Fallon, J. H., and Cahill, L. 1998. Hippocampal, but not amygdala, activity at encoding correlates with long-term, free recall of nonemotional information. *Proc. Natl. Acad. Sci. USA* **95:** 14506–14510.

Allison, T., McCarthy, G., Nobre, A., Puce, A., and Belger, A. 1994. Human extrastriate visual cortex and the perception of faces, words, numbers, and colors. *Cereb. Cortex* **5:** 544–554.

Amaral, D. G., and Insausti, R. 1990. Hippocampal formation. In *The Human Nervous System* (G. Praxinos, Ed.), pp. 711–755. Academic Press, San Diego.

Borowsky, I. W., and Collins, R. C. 1989. Metabolic anatomy of brain: A comparison of regional capillary density, glucose metabolism, and enzyme activities. *J. Comp. Neurol.* **288:** 401–413.

Brewer, J. B., Zhao, Z., Desmond, J. E., Glover, G. H., and Gabrieli, J. D. E. 1998. Making memories: Brain activity that predicts how well visual experience will be remembered. *Science* **281:** 1185–1187.

Buckner, R. L., Petersen, S. E., Ojemann, J. G., Miezin, F. M., Squire, L. R., and Raichle, M. E. 1995. Functional anatomical studies of explicit and implicit memory retrieval tasks. *J. Neurosci.* **15:** 12–29.

Carman, G. J., Drury, H. A., and Van Essen, D. C. 1995. Computational methods for reconstructing and unfolding the cerebral cortex. *Cereb. Cortex* **5:** 506–517.

Cohen, M. S. 1997. Parametric analysis of fMRI data using linear systems methods. *NeuroImage* **6:** 93–103.

Cohen, M. S., and DuBois, R. M. 1999a. Stability, repeatability, and the expression of signal magnitude in functional magnetic resonance imaging. *J. Magn. Reson. Imag.* **10:** 33–40.

Cohen, N. J., Ryan, J., Hunt, C., Romine, L., Wszalek, T., and Nash, C. 1999b. Hippocampal system and declarative (relational) memory: Summarizing the data from functional neuroimaging studies. *Hippocampus* **9:** 83–98.

Corbetta, M., Miezin, F. M., Dobmeyer, S., Shulman, G. L., and Petersen, S. E. 1991. Selective and divided attention during visual discriminations of shape, color, and speed: Functional anatomy by positron emission tomography. *J. Neurosci.* **11:** 2383–2402.

Dale, A. M., Fischl, B., and Sereno, M. I. 1999. Cortical surface-based analysis. I. Segmentation and surface reconstruction. *NeuroImage* **9:** 179–194.

Desgranges, B., Baron, J. C., and Eustache, F. 1998. The functional neuroanatomy of episodic memory: The role of the frontal lobes, the hippocampal formation, and other areas. *NeuroImage* **8:** 198–213.

Drury, H. A., Van Essen, D. C., Anderson, C. H., Lee, C. W., Coogan, T. A., and Lewis, J. W. 1996. Computerized mappings of the cerebral cortex: A multiresolution flattening method and a surface-based coordinate system. *J. Cognit. Neurosci.* **8:** 1–28.

Duvernoy, H. M. 1998. *The Human Hippocampus: Functional Anatomy, Vascularization, and Serial Sections with MRI.* Springer, Berlin.

Engel, S. A., Glover, G. H., and Wandell, B. A. 1997. Retinotopic organization in human visual cortex and the spatial precision of functional MRI. *Cereb. Cortex* **7:** 181–192.

Epstein, R., Harris, A., Stanley, D., and Kanwisher, N. 1999. The parahippocampal place area: Recognition, navigation, or encoding? *Neuron* **23:** 115–125.

Epstein, R., and Kanwisher, N. 1998. A cortical representation of the local visual environment. *Nature* **392:** 598–601.

Fernández, G., Brewer, J. B., Zhao, Z., Glover, G. H., and Gabrieli, J. D. 1999. Level of sustained entorhinal activity at study correlates with subsequent cued-recall performance: A functional magnetic resonance imaging study with high acquisition rate. *Hippocampus* **9:** 35–44.

Fernández, G., Weyerts, H., Schrader-Bolsche, M., I., T., Smid, H. G., Tempelmann, C., Hinrichs, H., Scheich, H., Elger, C. E., Mangun, G. R., and Heinze, H. J. 1998. Successful verbal encoding into episodic memory engages the posterior hippocampus: A parametrically analyzed functional magnetic resonance imaging study. *J. Neurosci.* **18:** 1841–1847.

Fischl, B., Sereno, M. I., and Dale, A. M. 1999. Cortical surface-based analysis. II. Inflation, flattening, and a surface-based coordinate system. *NeuroImage* **9:** 195–207.

Fletcher, P. C., Frith, C. D., Grasby, P. M., Shallice, T., Frackowiak, R. S., and Dolan, R. J. 1995. Brain systems for encoding and retrieval of auditory–verbal memory. An in vivo study in humans. *Brain* **118:** 401–416.

Fried, I., MacDonald, K. A., and Wilson, C. L. 1997. Single neuron activity in human hippocampus and amygdala during recognition of faces and objects. *Neuron* **18:** 753–765.

Gabrieli, J. D. E., Brewer, J. B., Desmond, J. D., and Glover, G. H. 1997. Separate neural bases of two fundamental memory processes in the human medial temporal lobe. *Science* **276:** 264–266.

Insausti, R., Juottonen, K., Soininen, H., Insausti, A., Partanen, K., Vainio, P., Laakso, M., and Pitkanen, A. 1998. MR volumetric analysis of the human entorhinal, perirhinal, and temporopolar cortices. *Am. J. Neuroradiol.* **19:** 659–671.

Jezzard, P., and Balaban, R. S. 1995. Correction for geometric distortion in echo planar images from B0 field variations. *Magn. Reson. Med.* **34:** 65–73.

Kanwisher, N., McDermott, J., and Chun, M. M. 1997. The fusiform face area: A module in human extrastriate cortex specialized for face perception. *J. Neurosci.* **17:** 4302–4311.

Kapur, S., Craik, F. I., Tulving, E., Wilson, A. A., Houle, S., and Brown, G. M. 1994. Neuroanatomical correlates of encoding in episodic memory: levels of processing effect. *Proc. Natl. Acad. Sci. USA* **91:** 2008–2011.

Maguire, E. A., Burgess, N., Donnett, J. G., Frackowiak, R. S., Frith, C. D., and O'Keefe, J. 1998. Knowing where and getting there: A human navigation network. *Science* **280:** 921–924.

Maguire, E. A., Frackowiak, R. S., and Frith, C. D. 1997. Recalling routes around London: Activation of the right hippocampus in taxi drivers. *J. Neurosci.* **17:** 7103–7110.

Mai, J. K. 1997. *Atlas of the Human Brain.* Academic Press, San Diego.

McCarthy, G. 1995. Functional neuroimaging of memory. *Neuroscientist* **1:** 155–163.

Milner, B. 1958. Psychological defects produced by temporal lobe excision. *Res. Publ. Assoc. Nerv. Ment. Dis.* **36:** 244–257.

O'Keefe, J., and Nadel, L. 1978. *The Hippocampus as a Cognitive Map.* Oxford Univ. Press, London.

Ouchi, Y., Nobezawa, R., Okada, H., Yoshikawa, E., Futatsubashi, M., and Kaneko, M. 1998. Altered glucose metabolism in the hippocampal head in memory impairment. *Neurology* **51:** 136–142.

Rausch, R., Henry, T. R., Ary, C. M., Engel, J. J., and Mazziotta, J. 1994. Asymmetric interictal glucose hypometabolism and cognitive performance in epileptic patients. *Arch. Neurol.* **51:** 139–144.

Rolls, E. T. 1996. A theory of hippocampal function in memory. *Hippocampus* **6:** 601–620.

Rolls, E. T., and O'Mara, S. M. 1995. View-responsive neurons in the primate hippocampal complex. *Hippocampus* **5:** 409–424.

Schwartz, E. 1990. Computer aided neuroanatomy of macaque visual cortex. In *Computational Neuroscience* (E. Schwartz, Ed.), pp. 295–315. MIT Press, Cambridge, MA.

Sereno, M. I., Dale, A. M., Reppas, J. B., Kwong, K. K., Belliveau, J. W., Brady, T. J., Rosen, B. R., and Tootell, R. B. 1995. Borders of multiple visual areas in humans revealed by functional magnetic resonance imaging. *Science* **268:** 889–893.

Shallice, T., Fletcher, P., Frith, C. P., Grasby, P., Frackowiak, R. S., and Dolan, R. J. 1994. Brain regions associated with acquisition and retrieval of verbal episodic memory. *Nature* **368:** 633–635.

Squire, L. R. 1992. Memory and the hippocampus: A synthesis from findings with rats, monkeys, and humans. *Psychol. Rev.* **99:** 195–231.

Stein, D. J., Buchsbaum, M. S., Hof, P. R., Siegel, B. V., Jr., and Shihabuddin, L. 1998. Greater metabolic rate decreases in hippocampal formation and proisocortex than in neocortex in Alzheimer's disease. *Neuropsychobiology* **37:** 10–19.

Stern, C. E., Corkin, S., González, R. G., Guimaraes, A. R., Baker, J. R., Jennings, P. J., Carr, C. A., Sugiura, R. M., Vedantham, V., and Rosen, V. 1996. The hippocampal formation participates in novel picture encoding: Evidence from functional magnetic resonance imaging. *Proc. Natl. Acad. Sci. USA* **93:** 8660–8665.

Stern, C. E., and Hasselmo, M. E. 1999. Bridging the gap: Integrating cellular and functional magnetic resonance imaging studies of the hippocampus. *Hippocampus* **9:** 45–53.

Swanson, L. W., Wyss, J. M., and Cowan, W. M. 1978. An autoradiographic study of the organization of intrahippocampal association pathways in the rat. *J. Comp. Neurol.* **181:** 681–715.

Teo, P. C., Sapiro, G., and Wandell, B. A. (1998). Segmenting cortical gray matter for functional MRI visualization. In *IEEE 6th International Conference on Computer Vision, New Delhi, India,* pp. 292–297.

Tulving, E., Markowitsch, H. J., Kapur, S., Habib, R., and Houle, S. 1994a. Novelty encoding networks in the human brain: Positron emission tomography data. *NeuroReport* **5:** 2525–2528.

Tulving, E., Kapur, S., Markowitsch, H. J., Craik, F. I., Habib, R., and Houle, S. 1994b. Neuroanatomical correlates of retrieval in episodic memory: Auditory sentence recognition. *Proc. Natl. Acad. Sci. USA* **91:** 2012–2015.

Tulving, E., Markowitsch, H. J., Craik, F. E., Habib, R., and Houle, S. 1996. Novelty and familiarity activations in PET studies of memory encoding and retrieval. *Cereb. Cortex* **6:** 71–79.

Ungerleider, L. G. 1995. Functional brain imaging studies of cortical mechanisms for memory. *Science* **270:** 769–775.

Van Essen, D. C., and Drury, H. A. 1997. Structural and functional analyses of human cerebral cortex using a surface-based atlas. *J. Neurosci.* **17:** 7079–7102.

Wagner, A. D., Schacter, D. L., Rotte, M., Koutstaal, W., Maril, A., Dale, A. M., Rosen, B. R., and Buckner, R. L. 1998. Building memories: Remembering and forgetting of verbal experiences as predicted by brain activity. *Science* **281:** 1188–1191.

Wandell, B. A., Engel, S. A., and Hel-Or, H. Z. 1996. Creating images of the flattened cortical sheet. *Invest. Ophthalmol. Visual Sci.* **37:** S1081.

Wong, O., Zeineh, M., Strojwas, M., Small, G., and Bookheimer, S. 1999. Activation patterns during encoding and retrieval of easy word-pairs in normal elderly individuals. *Soc. Neurosci. Abstr.* **25:** 295.

Woods, R. P., Dapretto, M., Sicotte, N. L., Toga, A. W., and Mazziotta, J. C. 1999. Creation and use of a Talairach-compatible atlas for accurate, automated, nonlinear intersubject registration, and analysis of functional imaging data. *Hum. Brain Mapp.* **8:** 73–79.

Woods, R. P., Grafton, S. T., Holmes, C. J., Cherry, S. R., and Mazziotta, J. C. 1998. Automated image registration. I. General methods and intrasubject, intramodality validation. *J. Comput. Assisted Tomogr.* **22:** 139–152.

Zola-Morgan, S., Squire, L. R., and Amaral, D. G. 1986. Human amnesia and the medial temporal region: Enduring memory impairment following a bilateral lesion limited to field CA1 of the hippocampus. *J. Neurosci.* **6:** 2950–2967.